Supporting Information

Harnessing NMR relaxation interference effects to characterize supramolecular assemblies

Gogulan Karunanithy, Arjen Cnossen, Henrik Muller, Martin D. Peeks, Nicholas H. Rees, Timothy D. W. Claridge, Harry L. Anderson and Andrew J. Baldwin

S.1 Synthesis of porphyrins

Six porphyrin derivatives were considered here: **P1** (R = *t*-Bu), ***l*-P2** (R = *t*-Bu), ***c*-P6** (R = THS and R = C_8H_{17}), ***c*-P6•T6** (R=THS) and ***l*-P6** (R=THS). The R groups are attached at the meta positions of the aryl rings (Main article Figure 1). ***c*** and ***l*** denote cyclic and linear assemblies respectively. Porphyrin compounds were prepared using previously described protocols.[1–3]

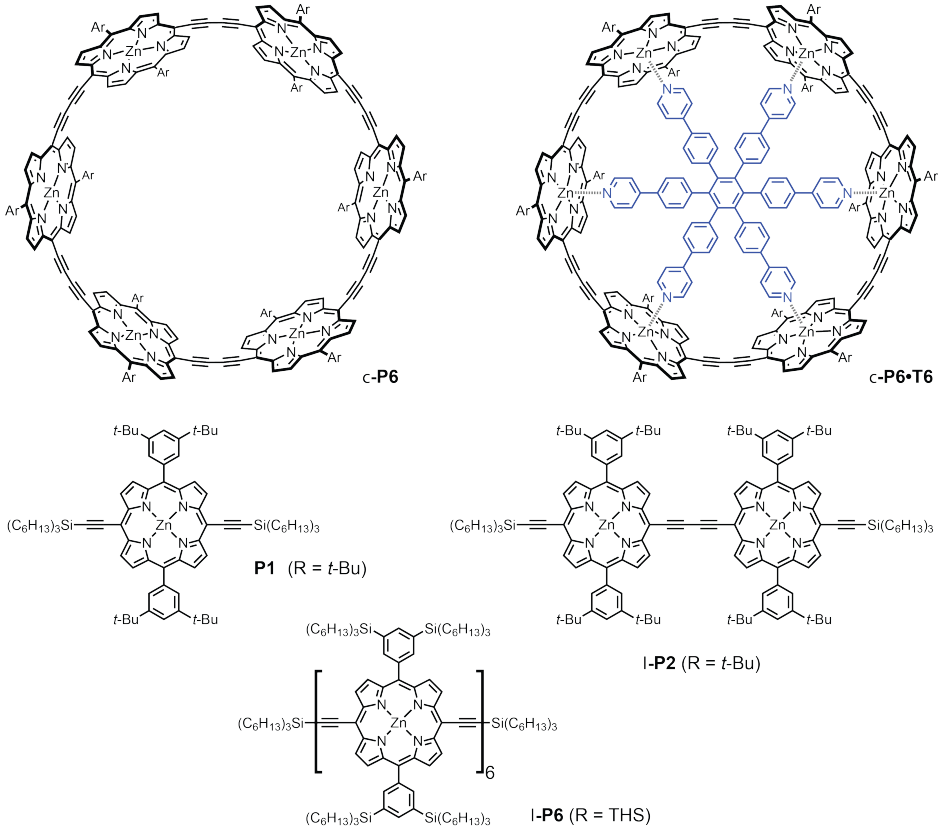

Figure S1 Full structures for the six porphyrin derivatives considered.

S.2 Relaxation Measurements

Relaxation measurements for α and β coupled spin where carried out on 7.1 T (300 MHz), 14.1 T (600 MHz), 17.6 T (750 MHz) and 22.3 T (950 MHz) narrow bore solution-state NMR spectrometers. All spectrometers were equipped with room temperature probes and the experiments were carried out at 298 K. The spectrometers were operating with Varian, GE Omega and Bruker operating systems and so pulse sequences for all formats are available on request. The number of CPMG elements (n) for each sample was varied so that for the highest value of n the intensity of the peaks dropped to approximately $\frac{1}{3}$ of their maximum value. A typical experiment employed a recycle delay of 2 s, acquisition time 2 s, 16 dummy scans, 8 transients per 1D and 16 different values for n. Some values of n are repeated for error analysis and the order in which the values of n were carried out was randomized to minimise any systematic effects. All spectra were phased and Fourier transformed using NMRPipe[4] and exported for analysis.

S.3 Data Analysis

It is not possible to obtain reliable intensities through summing the signal due to the degree of overlap between the two components of the doublet (Figure S2B). Instead we note that the peak function describing the central position of the resonance and its shape will not vary with *n*. To this end, we represent the doublets as the sum of two Pseudo-Voigt functions $P(\omega,\omega_0,\Delta,f)$ in which each is characterised by three parameters; a peak centre ω, a peak width Δ and a Gauss-to-Lorentz mixing factor *f*.

$$z(\omega,\omega_0,\Delta)=\frac{\omega-\omega_0}{\Delta},\quad L(\omega,\omega_0,\Delta)=\frac{1}{1+z(\omega,\omega_0,\Delta)^2},\quad G(\omega,\omega_0,\Delta)=e^{-\ln(2)z(\omega,\omega_0,\Delta)^2}$$
$$P(\omega,\omega_0,\Delta,f)=(fL(\omega,\omega_0,\Delta)+(1-f)G(\omega,\omega_0,\Delta)$$

The decay of the two peaks is then modelled by multiplying each function with a single exponential decay constant such that the spectrum at any given time is given by:

$$S(\omega,t)=P(\omega,\omega_{I\_S_\alpha},\Delta_{I\_S_\alpha},f_{I\_S_\alpha})e^{-tR_2^{I\_S_\alpha}}+P(\omega,\omega_{I\_S_\beta},\Delta_{I\_S_\beta},f_{I\_S_\beta})e^{-tR_2^{I\_S_\beta}}$$

The entire dataset of spectra as a function of frequency and time is analysed globally to obtain the 6 peak shape parameters and 2 rate constants. This procedure is illustrated in Figure S2 showing the comparison between raw and simulated data for two time points of one experiment (A). The decay of the peaks obtained from this method differs from the more usual method of simply taking the

integral. The difference between the two rates is illustrated in (B). Code to process data in this way was written in python and is available on request.

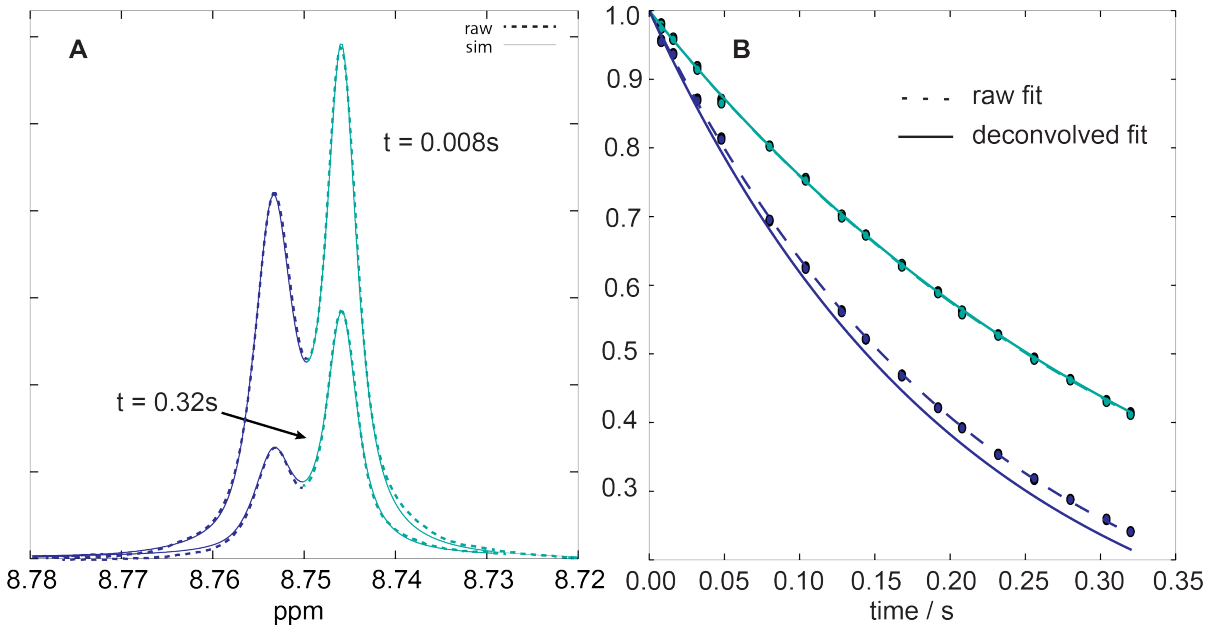

Figure S2 A. Fitted (solid lines) and raw (dotted lines) spectra of an I spin doublet at two different relaxation times. **B.** The expected signal intensities from the fitting (solid) are not in agreement with the intensities obtained from taking the peak height (dotted). The fitted intensities are the more reliable intensity measure as overlap effects are removed.

S.4 Rectangular Pulses for semi-selective refocusing

In this study semi-selective refocusing is achieved through the use of low power rectangular (constant amplitude) pulses rather than shaped pulses. Rectangular pulses are able to achieve a 180° flip in much shorter time than shaped pulses and consequently a larger range of time points may be interrogated before the transverse coherence decays. The difference in time for on resonance inversion is compared in Figure S3A and B. The selective rectangular pulses will be ca. 6 times shorter than optimised inversion pulses such Q3 or REBURP1 (Figure S3B).

The pulses are calibrated such that the on-resonance pulse undergoes a 180° flip whilst the scalar coupled partner undergoes a null pulse (Figure S3C). This is achieved by setting the pulse time (pw_{sel}) of the selective 180° pulse according to $pw_{sel} = \sqrt{3}/2\Delta\nu$ where $\Delta\nu$ is the difference in frequency (in Hz) between the spin of interest and its scalar coupled partner. The pulse is placed on resonance with the spin of interest and the power must be calibrated so that the spin undergoes a 180° flip during a pulse of this length (Figure S3D, E and F). A soft rectangular pulse of this type will have residual effects on the spectrum outside the region of interest, but it will effectively decouple the

spins of interest. Pulse times employed for the selective 180° pulses depend on the frequency difference of the samples investigated, but were approximately 1.7 ms at 600 MHz, 1.4 ms at 750 MHz and 1.1 ms at 950 MHz.

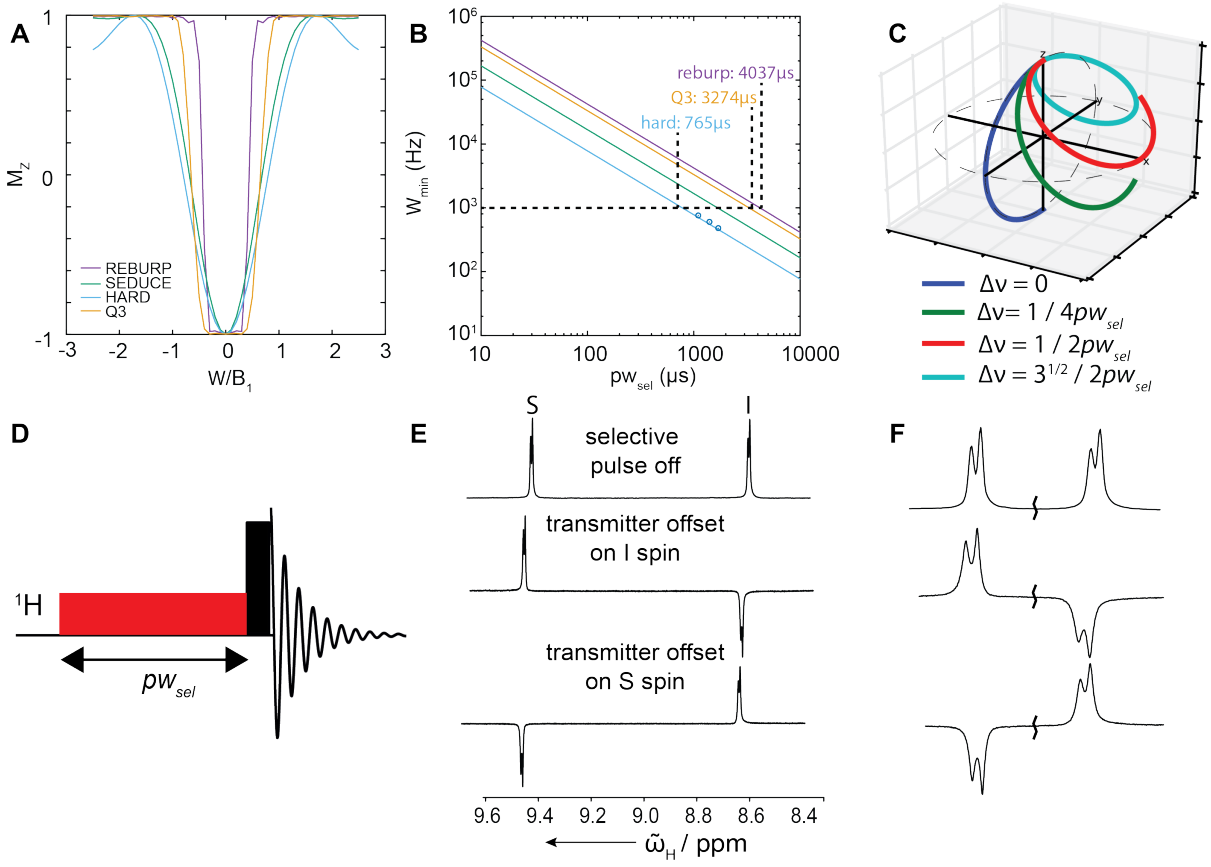

Figure S3 A. The effects of applying pulses of various shapes on a single spin initially at equilibrium as a function of offset Ω and B_1 field for commonly used pulse shapes. The REBURP1 and Q3 are more selective than SEDUCE or rectangular pulses. **B.** The offset between spins where on resonance experiences inversion, and 1% excitation is felt at the specified offset, as a function of pulse duration for the various pulse shapes. The selective rectangular pulses have a duration ca. 5x shorter than those with more complex shapes making them highly amenable to measurements of this type, particularly when rapid relaxation is expected. **C.** The trajectory of magnetisation in the rotating frame during a rectangular pulse as a function of frequency offset. The on resonance spin undergoes a 180° flip whereas the spin which is off resonance by the optimal value effectively experiences no pulse. **D.** A pulse sequence used to ensure that the selective pulse has been calibrated correctly consists of a selective 180° pulse (shown in red) and a 'hard' rectangular 90° pulse (black) executed at maximum power and minimum duration. As shown in **E.** and **F.** when the selective pulse is calibrated correctly and placed on resonance with one of the spins of interest there will be a 180° phase shift between the two spins as the off resonance spin effectively experiences a null during the first pulse.

S.5 Summary of Redfield calculations of relaxation rates for AX_n spin systems

Relaxation rates of the difference coherences can be calculated as follows using the approach of Redfield. We consider here dipolar and CSA interactions between spins ½ and the correlations between the two. The strengths of the two interactions are given respectively by:

$d = \frac{\mu_0 \gamma_I \gamma_S \hbar}{4\pi r_{IS}^3}$ and $c = \gamma_I B_0 \Delta\sigma$

A_k	A_l^d	F_k	$S_{k/l}$	$w(A_k)$
I_zS_Z	I_zS_z	$(1\text{-}3\cos^2(\theta))$	d	0
I_+S_-	I_-S_+	$¼(1\text{-}3\cos^2(\theta))$	d	$\omega_I\text{-}\omega_S$
I_+S_-	I_-S_+	$¼(1\text{-}3\cos^2(\theta))$	d	$\omega_I\text{-}\omega_S$
I_zS_+	I_zS_-	$^3/_2 \sin(\theta)\cos(\theta)\exp(-i\phi)$	d	ω_S
I_zS_-	I_zS_+	$^3/_2 \sin(\theta)\cos(\theta)\exp(+i\phi)$	d	ω_S
I_+S_z	I_-S_z	$^3/_2 \sin(\theta)\cos(\theta)\exp(-i\phi)$	d	ω_I
I_-S_z	I_+S_z	$^3/_2 \sin(\theta)\cos(\theta)\exp(+i\phi)$	d	ω_I
I_+S_+	I_-S_-	$¾ \sin^2(\theta) \exp(-2i\phi)$	d	$\omega_I+\omega_S$
I_-S_-	I_+S_+	$¾ \sin^2(\theta) \exp(2i\phi)$	d	$\omega_I+\omega_S$
I_z	I_z	$^1/_3(1\text{-}3\cos^2(\theta))$	c	0
I_+	I_-	$¼ \sin(2\theta)\exp(-i\phi)$	c	ω_I
I_-	I_+	$¼ \sin(2\theta)\exp(+i\phi)$	c	ω_I

Table 1 Summary of the spin state terms contained in the dipolar and chemical shift anisotropy Hamiltonians.

where γ is the gyromagnetic ratio of the relevant spin, μ_0 is the magnetic constant, r_{IS} is the distance between spins I and S, $\Delta\sigma$ is the chemical shift anisotropy (CSA) in ppm and B_0 is the static magnetic field strength. The relaxation rate of a given coherence ρ_i, such as I_z or I_x due to another, ρ_j, is obtained from Redfield's equation:

$$R_{\rho_i\rho_j} = \sum_{k,l} \frac{1}{2} S_l^\dagger S_k \frac{<\rho_i|[A_l^\dagger[A_k,\rho_j]]>}{<\rho_i|\rho_j>} \overline{F_l^\dagger F_k} J(\omega(A_k))$$

The sum here extends to all combinations of spin operators in the appropriate Hamiltonian, subject to the secular approximation that requires $\omega(A_k)+\omega(A_l)=0$ where $\omega(A_k)=-\omega(A_k^d)$, and $F_l=F_k^*$. In the case of dipolar and CSA interactions, the relevant terms are summarised in table 1. For an AX spin system, as is considered here, there will be 12 terms in the combined chemical shift anisotropy and dipolar Hamiltonians, leading to the sum extending over 144 possible contributions to the relaxation rate.

Each individual term (A_k) is evaluated with respect to the Hermitian conjugate (A_l^d) of all possible terms. A normalised spectral density function for isotropic rotational motion is:

$$J(\omega) = \frac{2}{5}\frac{\tau_c}{1+\omega^2\tau_c^2}$$

and the ensemble averaged spatial terms are evaluated from

$$\overline{F_l^\dagger F_k} = \frac{1}{4\pi}\int_0^{2\pi}\int_0^{\pi} F_l^\dagger F_k \sin\theta\, d\theta\, d\phi$$

In general, the auto relaxation rate where ρ_i=ρ_j for any single quantum coherence from an AX_n spin system where the 'A' is a single quantum coherence and the 'X' are the complete set of α and β spin states that can accompany the coherence will be given by the following result:

$$R_2^{S\_\Pi I_{\alpha/\beta}} = \left(\left(1+\left(\frac{2j^2}{j_{max}}-1\right)P_2^0(\cos\theta_{DD})\right)2j_{max}R_D^2 + R_C^2 + 4jP_2^0(\cos\theta_{CS})R_DR_C\right)f + 2j_{max}R_D^2 f_{ADD}$$

where we make use of the following 4 definitions:

$$R_D = \frac{d}{2\sqrt{5}},\ \ R_C = \frac{c}{3\sqrt{5}},\ \ f = 4J(0)+3J(\omega_S),\ \ f_{ADD} = 3J(\omega_I)+J(\omega_S-\omega_I)+6J(\omega_S+\omega_I)$$

and $P_2^0(x) = \frac{1}{2}\left(3x^2-1\right)$, θ_{DD} is the angle between dipolar vectors (assumed constant here) and θ_{CS} is the angle between the principal axis of the chemical shift tensor and the inter nuclear vector for the dipolar coupling. The net spin of the coupled spins for the coherence of interest is *j* and j_{max} is maximum possible angular momentum for the coupled spins. For example, for a coherence of the form $S\_I_\alpha I_\beta$, j_{max} would be 3/2 and *j* would be ½. In the present manuscript, the method is applied to an AX spin system, and so S_I_α and S_I_β are the relevant relaxation rates where j_{max}=*1/2* and *j=+1/2* or *-1/2*. Using this equation, the method can be applied to any spin system of the type A_mX_n. The relaxation rates will need to be further modified for more complicated spin systems and additional dynamics such as methyl group rotation.

S.6 Global analysis of relaxation data

A set of R_2 measurements for I_-S_α, I_-S_β, $I_\alpha S_-$ and $I_\beta S_-$ were obtained as described above for each porphyrin sample as a function of magnetic field strength. The relaxation rates can be back calculated from the appropriate relaxation equations as a function of τ_c and $\Delta\sigma_{CSA}$ of the S spin and σ_{CSA} of the I spin, and the angle between the dipolar vector and CSA principal axis. These parameters were globally minimised to obtain the fitted curves (Figure 3, Figure S4A). An additional term corresponding to $R'_D{}^2 f_{ADD}$ was also included to account for dipolar relaxation due to remote protons, where the distance in used to calculate R_D is defined by the relevant inter-proton distance.

Uncertainties in parameters were determined using a bootstrapping procedure. This involves creating a number of synthetic datasets by randomly selecting data points from the original sample with replacement. The same optimisation is then run on the synthetic dataset to give values for the fitting parameters. This process is then repeated ca. 1000 times enabling a histogram of fitted values can be plotted. The standard deviation in the bootstrap values for the fitting parameters can be used as an estimate for the error (Figure S4B). In the analysis we obtain the cosine of the angle. The specific angle stated is the solution between 90 and 180° for numerical convenience.

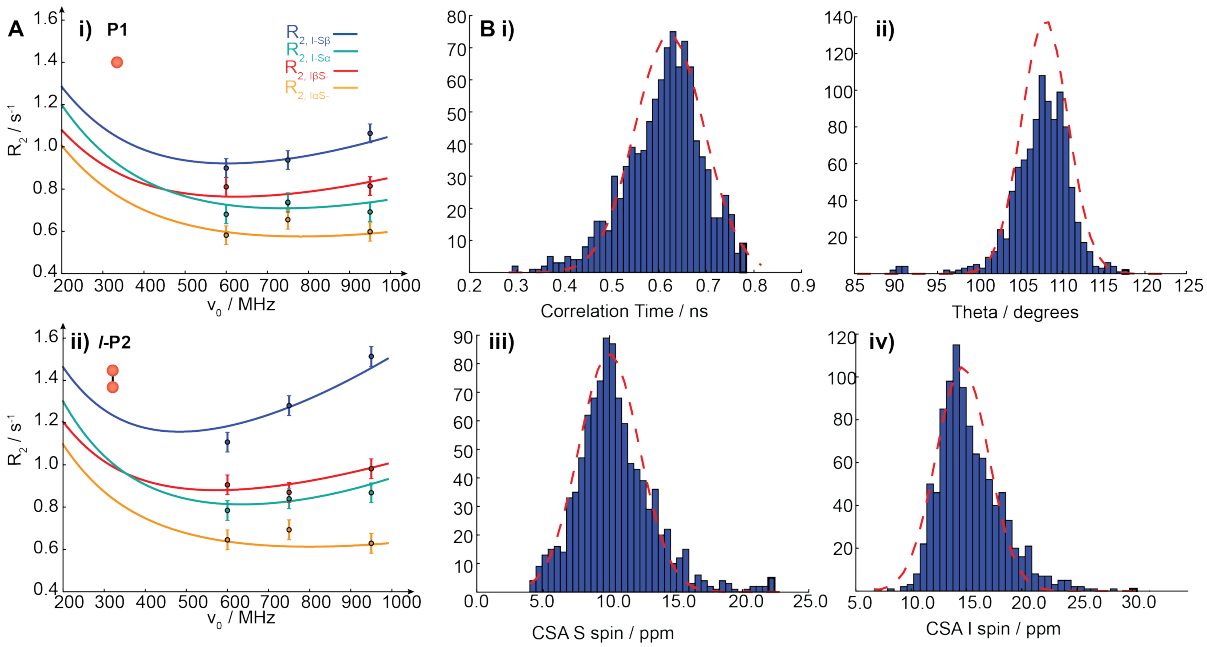

Figure S4 A. Relaxation rates as a function of magnetic field strength, and global fits for monomeric and dimeric porphyrins. **B.** The uncertainty distributions in parameters from a bootstrap analysis. The standard deviation of the histogram is an estimate of the uncertainty in the fitting parameter.

S.7 NMR Translational diffusion measurements

The diffusion coefficients were measured at 11.74 T (500 MHz) on an AVII spectrometer (Bruker) at 298 K. A convection-compensating double-stimulated echo experiment (DSTE) using bipolar gradients was used. The diffusion time Δ was 235.40 ms, and the gradient pulse length was 3 ms. A linear gradient increment was used. The sample contained **P1**, ***l*-P6** and ***c*-P6•T6** in $CDCl_3$. Diffusion coefficients were determined by an exponential fit to the integrated area of resonances of each component using the Stejskal-Tanner equation.[5]

$$S_i = S_0 e^{-\gamma^2 G^2 \delta^2 (\Delta - \frac{\delta}{3}) D_T}$$

Where S_i is the measured signal intensity, S_0 is the maximum signal intensity in the absence of gradient dephasing, γ is the gyromagnetic ratio, Δ is the diffusion time, δ is the gradient pulse length and G is the gradient field strength. A representative decay curve is shown in Figure S5B.

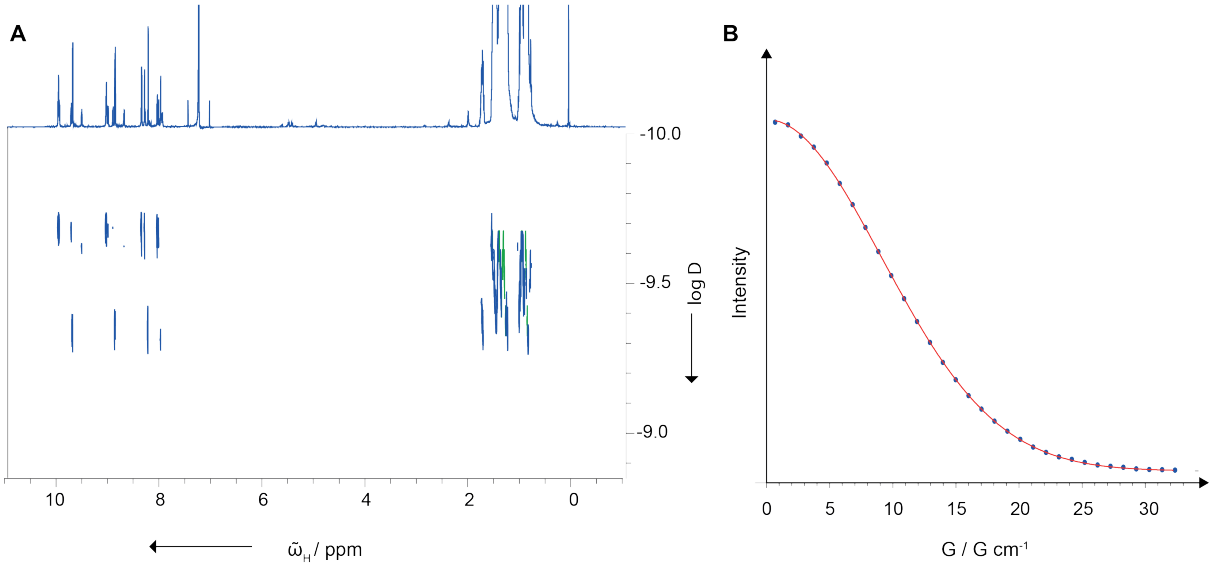

Figure S5 A. DOSY spectrum from which **P1, *l*-P6 and *c*-P6•T6** can be identified. **B.** Example of intensity decrease with increased gradient field strength (G) from which a diffusion coefficient can be fitted for each of the molecules.

S.8 Calculation of rotational correlation times for linear *l*-P6 from translational diffusion

To obtain a correlation time for the linear molecule ***l*-P6**, it was necessary to include a correction to account for its anisotropic diffusion. The diffusion constant for a molecule is related to the friction factor, F, through the relationship:

$D = \frac{k_B T}{F}$ where for a rod of length *L* and radius *R* the friction factor is given by: $F = 3\pi\eta L(\ln\left(\frac{L}{R}\right) - 0.3)^{-1}$. The radius of a rod-like molecule can be determined from a known length and its translational diffusion coefficient from $R = L(\exp\left(0.3 + \frac{3\pi\eta LD}{kT}\right))^{-1}$. By equating the volume of a sphere to the volume of the rod, we can obtain the effective spherical radius of the rod, in terms of the viscosity, the observed diffusion coefficient (D) and the length of the rod.

$$r_{sphere} = L\left(\frac{3}{4}\exp\left(-\frac{6}{10} - \frac{6\pi\eta LD}{kT}\right)\right)^{1/3}$$

From the effective spherical radius, a correlation time can be determined. The viscosity of $CDCl_3$ at 298 K is 0.542 mPa.[6]

S.9 Solid-state NMR determination of ^{13}C CSA

For the monomeric porphyrin, it was possible to independently measure the CSA using solid-state NMR spectroscopy as described in the main text. The intensity of the spinning side bands was measured as a function of spinning rate. A cross-polarisation (CP) element was used to enhance ^{13}C sensitivity and spectra were recorded at magic angle spinning (MAS) frequencies of 1 kHz, 3 kHz and 10 kHz.

Individual ^{13}C resonances from the carbon nuclei attached to I and S protons could be resolved in the ^{13}C MAS spectra (Main article Figure 4E) and were correlated to the appropriate ^{1}H resonance using a ^{1}H-^{13}C HSQC spectrum. For the Herzfeld-Berger analysis the 3 kHz spinning speed was chosen as the overlap between resonances was minimal while yet still enabling resolution of a number of side band resonances.

By fitting the sideband pattern associated with a particular resonance in a solid-state NMR spectrum using a Herzfeld-Berger analysis[7] it is possible to derive the CSA of that resonance. Solid-state NMR experiments were carried out on a **P1** sample (with t-Bu side groups) with a 9.4 T (400 MHz) Bruker Avance III HD spectrometer equipped with a room-temperature 4 mm MAS probe. The CSAs of the carbon nuclei attached to the I and S protons were found to be 124.0±6.3 ppm and 124.8±2.7 ppm respectively. These values compare favourably to those from DFT calculations (section S.10). The same measurements were not possible directly on ^{1}H due to resonance overlap.

S.10 DFT Calculations

The chemical shift tensor was estimated using DFT calculations. Using the software Gaussian09[8], an optimised structure is generated. Once the geometry is optimised, the shielding tensor is calculated, enabling isotropic and anisotropic components to be determined. All DFT calculations were carried out using the B3LYP density functional with the 6-31G(d) basis set.

The experimental and calculated isotropic chemical shifts of a database of small organic compounds are shown together with values calculated for **P1** (Figure S6). The correlation between the two values is excellent over this range.

Calculations were performed on the range of side groups used in the NMR study to confirm that these have a limited impact on the measured CSAs (Table S2). There is excellent agreement between the experimental ^{13}C CSA measurements (section S.9) and those calculated using this method, validating the calculation method. The agreement between the ^{1}H CSA determined using the relaxation measurements that are the main focus of this paper (Figure 4) and the calculations is similarly excellent.

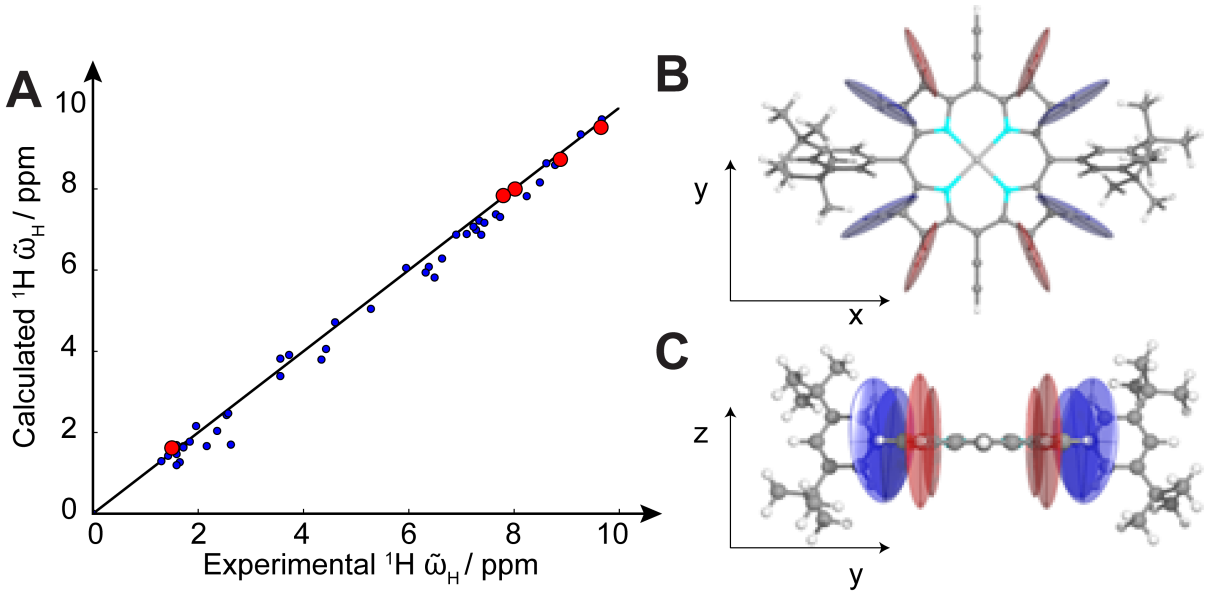

Figure S6 A. Correlation plot of calculated and experimental isotropic chemical shifts using DFT with B3LYP / 6-31G(d). Blue dots indicate experimental and calculated chemical shifts for 24 small organic molecules where experimental chemical shifts are taken form the Spectral Database for Organic Compounds.[9] Red dots indicate experimental and calculated chemical shifts for **P1** (R = *t*-Bu). **B/C.** Ellipsoid representations of the calculated CSA tensors of the I (blue) and S (red) spins . The ellipsoids are rotated to align with the eigenvectors of the chemical shielding tensor and their axes are scaled to the corresponding eigenvalue. Eigenvalues and eigenvectors are calculated from the symmetric component of the computed chemical shielding tensor and eigenvalues are subtracted from the isotropic shift of TMS calculated at the same level of theory. The most deshielded component of the tensor for I and S spins is perpendicular to the plane of the porphyrin. The CSA from the DFT and

that measured experimentally from the relaxation interference measurements are in excellent agreement (Figure 4).

R =	I ^{1}H CSA / ppm	S ^{1}H CSA / ppm	I ^{13}C CSA / ppm	S ^{13}C CSA / ppm
t-Bu**	16.5±0.1	12.9±0.4	131.317±0.138	126.6±0.2
t-Bu	15.3±0.1	12.1±0.1	132.495±0.035	128.4±0.1
THS	14.1±0.4	13.0±0.1	132.368±0.227	128.3±0.5
OC_8H_{17}	14.8±0.1	11.8±0.1	132.820±0.185	128.2±0.1

**Includes THS groups on the terminal acetylenes – in all other cases this was replaced with a hydrogen atom.

Table 2 List of DFT derived CSAs in both ^{1}H and ^{13}C in the presence of different R groups.

S.11 Calculation of Intensity Ratios

Assuming lorentzian lineshapes, the normalised intensity of a peak as a function of frequency is given by:

$$I = \frac{R_2}{R_2^2 + (\omega - \omega_0)^2}$$

Where the peak is centered at frequency ω_0. The maximum intensity of a peak is thefore proportional to $\frac{1}{R_2}$. The R_2 contains a contribution from both intrinsic relaxation and magnetic field inhomogeneity. In the case of a doublet (e.g. $I_\alpha S_-$ and $I_\beta S_-$) the ratio of the maximum intensities is given by: $\frac{R_2^{I_\beta S_-}}{R_2^{I_\alpha S_-}}$.

As shown in Figure S7, in the presence of magnetic field inhomogeneity the intensity difference expected due to relaxation interference is largely obscured for small molecules that have correlation times on the picosecond timescale. However for large supramolecular assemblies that tumble on the nanosecond timescale, as exemplified by the porphyrin oligomers, significant differences in intensity can be detected by inspection of spectra, given a reasonably high CSA. The magnitude of the effect is amplified when using a higher static field strength (Figure S7 and main article Figure 3). Due to the dependence of the effect on correlation time, any factors that affect this e.g. a change in temperature, solvent viscosity or presence of local motion will also affect the ratio of intensities.

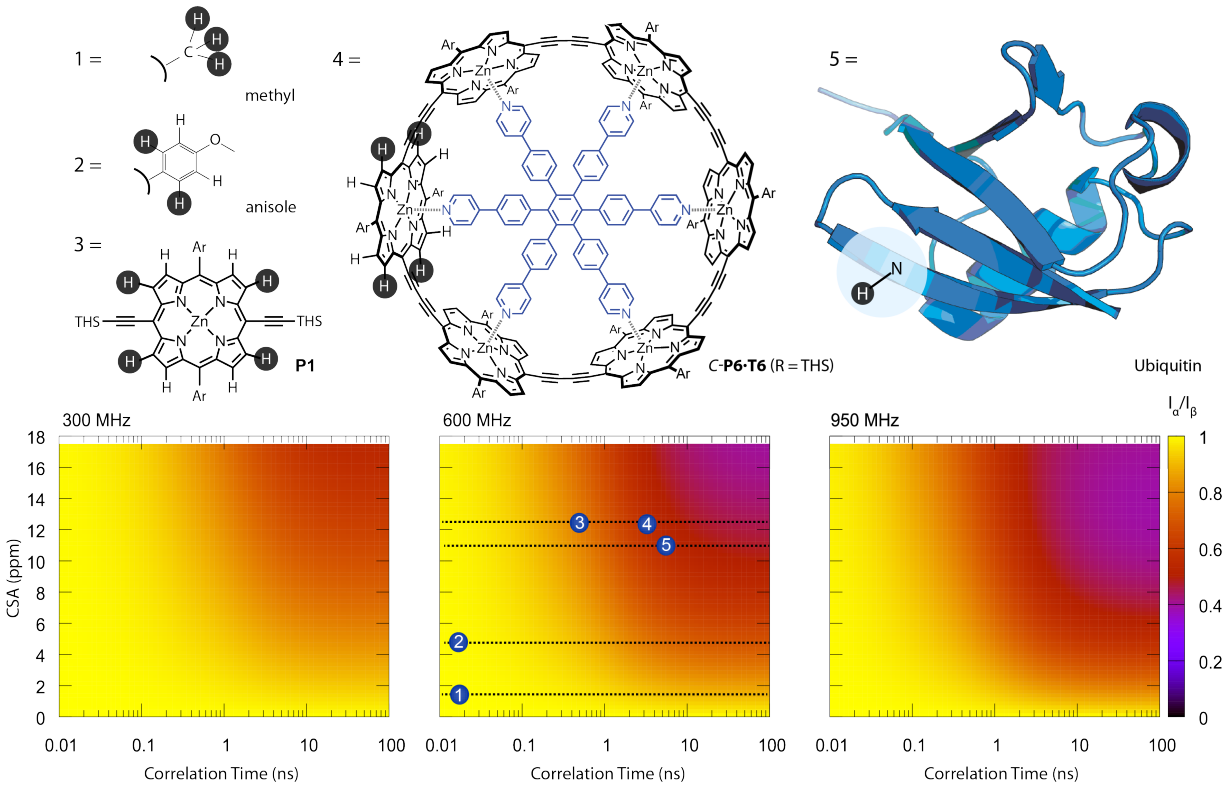

Figure S7 Heat maps showing the ratio of signal intensities for a single scalar coupled doublet intensities $\frac{I_\alpha}{I_\beta}$ for a range of molecules/substituents at magnetic field strengths corresponding to proton Lamor frequencies of 300, 600 and 950 MHz. The relaxation rate is calculated using the equations in the text assuming dipolar coupling to another proton at a distance of 2.5 Å with an angle of 90° between the dipolar and CSA principal axes, as was the case for the porphyrin oligomers. 1 s^{-1} inhomogeneous broadening has been added to reflect a typical experimental case, and so for a broad range of parameter space, the two components are of equal intensity (yellow). Specific CSA values for specific protons in functional groups are indicated (lines), including a CH3 group, aromatic protons in a substituted benzene ring, two porphyrins used in this study, and an amide proton, as frequently encounted in the context of proteins. The specific combinations of correlation time and CSA, for specific molecules are expliticlty numbered. The magnitude of the effect will vary with the molecule but these values serve as a qualitative guide for when the effect should be anticipated. In general, increasing the effective correlation time above the point where the line width is limited by inhomogeneous broadening will render relaxation interference directly observable in NMR spectra. This can be accomplished by, for example, reducing local internal dynamics, increasing the overall molecular weight of the molecule, decreasing the temperature or increasing the viscosity.

Supplementary References

1 J. K. Sprafke, D. V Kondratuk, M. Wykes, A. L. Thompson, M. Hoffmann, R. Drevinskas, W.-H. Chen, C. K. Yong, J. Kärnbratt, J. E. Bullock, M. Malfois, M. R. Wasielewski, B. Albinsson, L. M. Herz, D. Zigmantas, D. Beljonne and H. L. Anderson, *J. Am. Chem. Soc.*, 2011, **133**, 17262–73.

2 P. N. Taylor, J. Huuskonen, R. T. Aplin, H. L. Anderson, J. Huuskonen, G. Rumbles and E.

Williams, *Chem. Commun.*, 1998, 909–910.

3 C. E. Tait, P. Neuhaus, M. D. Peeks, H. L. Anderson and C. R. Timmel, *J. Am. Chem. Soc.*, 2015, **137**, 8284–8293.

4 F. Delaglio, S. Grzesiek, G. Vuister, G. Zhu, J. Pfeifer and A. Bax, *J. Biomol. NMR*, 1995, **6**.

5 E. O. Stejskal and J. E. Tanner, *J. Chem. Phys.*, 1965, **42**, 288.

6 J. A. Dean, *Lange's Handbook of Chemistry*, McGraw-Hill, Inc, 1995.

7 J. Herzfeld and A. E. Berger, *J. Chem. Phys.*, 1980, **73**, 6021.

8 M. J. Frisch, G. W. Trucks, H. B. Schlegel, G. E. Scuseria, M. A. Robb, J. R. Cheeseman, G. Scalmani, V. Barone, B. Mennucci, G. A. Petersson, H. Nakatsuji, M. Caricato, X. Li, H. P. Hratchian, A. F. Izmaylov, J. Bloino, G. Zheng, J. L. Sonnenberg, M. Hada, M. Ehara, K. Toyota, R. Fukuda, J. Hasegawa, M. Ishida, T. Nakajima, Y. Honda, O. Kitao, H. Nakai, T. Vreven, J. A. Montgomery, Jr., J. E. Peralta, F. Ogliaro, M. Bearpark, J. J. Heyd, E. Brothers, K. N. Kudin, V. N. Staroverov, R. Kobayashi, J. Normand, K. Raghavachari, A. Rendell, J. C. Burant, S. S. Iyengar, J. Tomasi, M. Cossi, N. Rega, J. M. Millam, M. Klene, J. E. Knox, J. B. Cross, V. Bakken, C. Adamo, J. Jaramillo, R. Gomperts, R. E. Stratmann, O. Yazyev, A. J. Austin, R. Cammi, C. Pomelli, J. W. Ochterski, R. L. Martin, K. Morokuma, V. G. Zakrzewski, G. A. Voth, P. Salvador, J. J. Dannenberg, S. Dapprich, A. D. Daniels, Ö. Farkas, J. B. Foresman, J. V. Ortiz, J. Cioslowski, D. J. Fox, *Gaussian, Inc., Wallingford CT* 2009.

9 SDBSWeb: http://sdbs.db.aist.go.jp National Institute of Advanced Industrial Science and Technology (Japan), Accessed May 2015